# Faraday Discussions

Accepted Manuscript

This manuscript will be presented and discussed at a forthcoming Faraday Discussion meeting. All delegates can contribute to the discussion which will be included in the final volume.

**Register now to attend!** Full details of all upcoming meetings: http://rsc.li/fd-upcoming-meetings

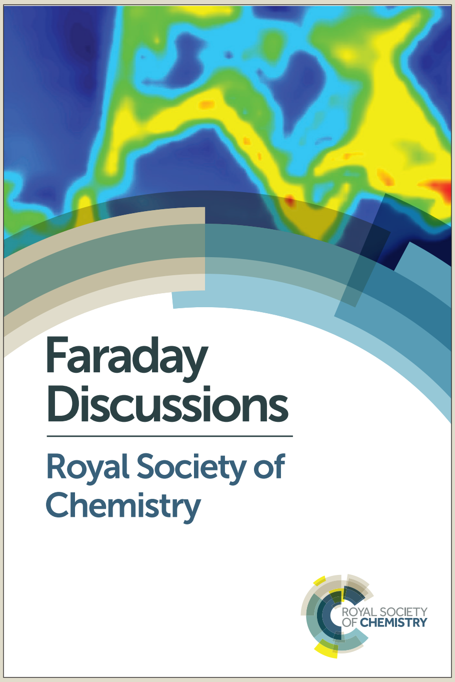

This is an *Accepted Manuscript*, which has been through the Royal Society of Chemistry peer review process and has been accepted for publication.

*Accepted Manuscripts* are published online shortly after acceptance, before technical editing, formatting and proof reading. Using this free service, authors can make their results available to the community, in citable form, before we publish the edited article. We will replace this *Accepted Manuscript* with the edited and formatted *Advance Article* as soon as it is available.

You can find more information about *Accepted Manuscripts* in the Information for Authors.

Please note that technical editing may introduce minor changes to the text and/or graphics, which may alter content. The journal's standard Terms & Conditions and the Ethical guidelines still apply. In no event shall the Royal Society of Chemistry be held responsible for any errors or omissions in this *Accepted Manuscript* or any consequences arising from the use of any information it contains.

ROYAL SOCIETY OF CHEMISTRY

www.rsc.org/faraday_d

# Electrochemistry at Single Molecule Occupancy in Nanopore-Confined Recessed Ring-Disk Electrode Arrays

Kaiyu Fu,[1] Donghoon Han,[2] Chaoxiong Ma,[1] and Paul W. Bohn[1,2*]

[1]Department of Chemistry and Biochemistry, University of Notre Dame, Notre Dame, IN 46556

[2]Department of Chemical and Biomolecular Engineering, University of Notre Dame, Notre Dame, IN 46556

[*]Author to whom correspondence should be addressed, *pbohn@nd.edu*

## ABSRACT

Electrochemical reactions at nanoscale structures possess unique characteristics, *e.g.* fast mass transport, high signal-to-noise ratio at low concentration, and insignificant ohmic losses even at low electrolyte concentrations. These properties motivate the fabrication of high density, laterally ordered arrays of nanopores, embedding vertically stacked metal-insulator-metal electrode structures and exhibiting precisely controlled pore size and interpore spacing for use in redox cycling. These nanoscale recessed ring-disk electrode (RRDE) arrays exhibit current amplification factors, $AF_{RC}$, as large as 55-fold with $Ru(NH_3)_6^{2/3+}$, indicative of capture efficiencies at the top and bottom electrodes, $\Phi_{t,b}$, exceeding 99%. Finite element simulations performed to investigate the concentration distribution of redox species and to assess operating characteristics are in excellent agreement with experiment. $AF_{RC}$ increases as the pore diameter, at constant pore spacing, increases in the range 200 – 500 nm and as the pore spacing, at constant pore diameter, decreases in the range 1000 – 460 nm. Optimized nanoscale RRDE arrays exhibit a linear current response with concentration ranging from 0.1 μM to 10 mM and a small capacitive current with scan rate up to 100 V $s^{-1}$. At the lowest concentrations, the average pore occupancy is $\langle n \rangle \sim 0.13$ molecule establishing productive electrochemical signals at occupancies at and below the single molecule level in these nanoscale RRDE arrays.

# INTRODUCTION

The rapid development of nanofabrication techniques has enabled electrochemical experiments with electrodes in the nanoscale regime.[1, 2] Typically this has been realized by fabricating ultrasmall electrodes with critical dimensions below 100 nm that exhibit unique electrochemical properties, *e.g.* sigmoidal voltammetric response, negligible ohmic (*iR*) potential losses, and small intrinsic charging currents.[3, 4] Nanoelectrodes have also been employed to advantage in investigations of mass transport and electron transfer with enhanced temporal and spatial resolution.[5, 6] Many reports focus on the fabrication of single nanoelectrodes with characteristic sizes ranging from a few nanometers to > 100 nm,[7-9] however, when compared to macroscopic electrodes, or even microelectrodes, the current is limited, and achieving device-to-device reproducibility is challenging. Nanoelectrode ensembles (NEEs)[10, 11] and nanoelectrode arrays (NEAs)[12-14] have been fabricated to increase the measurable current while maintaining the large bandwidth benefits of nanoelectrodes.[15] Recently, we have explored massively parallel arrays of NEAs fabricated with dual electrodes embedded in nanopores and operated in redox cycling (RC) mode, either with or without supporting electrolyte.[16-21]

In RC mode, reversible electro-active species undergo successive oxidation and reduction reactions by cycling between two closely-spaced, independently-addressable electrodes, *i.e.* electroactive molecules that are oxidized at one electrode then move to the other electrode and are reduced, then they can move back to the anode and repeat the cycle.[22] Pioneering work on RC was accomplished with rotating ring-disc electrodes[23, 24] and interdigitated array electrodes[25-27], which used forced convection and the small size (5-50 μm, typ.) of the interelectrode gap, respectively, to amplify current. Bard and coworkers[28-30] extended the electrode spacing concept in an elegant way to directly detect current resulting from redox cycling of single molecules in a small volume trapped between a surface and a scanning electrochemical microscopy tip. Improvements in nanofabrication technology have made it possible to fabricate more precise RC systems, *e.g.* nanofluidic channels with closely parallel electrodes,[31, 32] nanogap electrodes enclosing attoliter volumes,[33] and nanopore-based arrays with recessed ring-disk electrodes[20] have all been designed for ultrasensitive electrochemical measurements. Nanopore-based electrodes constitute a special class of nanoscale RC systems, because redox species are confined and can become electrostatically trapped such that they react with both electrodes multiple times before diffusing out of the nanopore.

In order to produce nanopore-based RC systems with control over geometric parameters, such as pore size, density and interpore distance, advanced lithographic techniques, *e.g.*, electron-beam lithography (EBL) and focused ion beam (FIB) milling, have been employed. For example, Wolfrum and co-workers[34] reported an approach to high density nanopore electrode arrays by combining EBL and reaction ion etching (RIE). Recently, our group took advantage of FIB milling to fabricate high density (~ 2 x $10^9$ $cm^{-2}$) dual-ring nanopore electrode arrays which exhibit enhanced electrochemical performance.[21] However, these techniques are restricted by the need for serial-write lithography processes, employ expensive facilities, are time-consuming, and produce low throughput, so they are not well-suited to fabricating high density patterns at large scale.

Nanosphere lithography (NSL), also known as colloidal lithography, is based on the natural self-assembly of colloidal particle templates on substrates and was introduced by Fischer and Zingsheim in 1981.[35] Since then, by using smaller size nanospheres[36, 37] and well-designed coating methods, [38, 39] nanostructured arrays with elements smaller than 100 nm have been achieved with long-range order over large distances. We have used this procedure to develop sub-micrometer arrays with dual electrodes, demonstrating excellent sensitivity and selectivity in voltammetric measurements [17, 19]

Here, we extend the geometry of NSL-templated recessed ring-disk electrode (RRDE) arrays to small spacings (<500 nm) and large pore densities (up to $10^9$ pores $cm^{-2}$) and explore the dependence of voltammetric response on the geometry of the array, including pore size and inter-pore spacing, in order to produce structures capable of redox cycling under single molecule occupancy conditions. By varying the size of the nanospheres in the template and the exposure time to $O_2$ plasma etching, nanopore electrode arrays with a wide range of pore diameters (800 nm to 100 nm) and pore densities ($10^8$-$10^9$ pores $cm^{-2}$) have been achieved with good uniformity at large scale. The optimized RRDE arrays demonstrate high collection efficiency in RC mode, producing current amplification as large as 55-fold. At the lowest concentrations examined, this performance is sufficient to achieve electrochemical measurements at single molecule occupancy levels, *i.e.* signals are obtained from a parallel array of nanopores, each containing $\langle n \rangle \leq 1$ molecules, with the single molecule cycling between the lower (disk) and upper (ring) electrodes. The dependence of voltammetric behavior on the potential of the generator and collector electrodes, and the size and spacing of the nanopores in RC mode has been investigated experimentally and compared with the results of finite element simulations, showing that both pore diameter and pore density are important factors that govern transport-limited electron transfer and the corresponding current amplification. These structures also exhibit a linear current response over a wide range of analyte concentration and exhibit remarkably small capacitive currents, even at very fast scan rates.

## EXPERIMENTAL SECTON

*Chemicals and Materials.* Hexaammineruthenium chloride ($[Ru(NH_3)_6]Cl_3$), potassium chloride, sulfuric acid (95%), and hydrogen peroxide (30%) were obtained from Sigma-Aldrich and used as received. Deionized (DI) water was generated from a milli-Q Gradient water purification system (Millipore). Photoresist AZ5214E (AZ Electronic Materials) and polydimethylsiloxane (PDMS) (Dow Corning) were used according to the manufacturers' specifications.

*Device Fabrication.* High density RRDE arrays were fabricated by using photolithography, layer-by-layer deposition, nanosphere lithography (NSL), and multiple reactive ion etching (RIE), similar to previously reported procedures.[20] A glass slide was cleaned in piranha solution (3:1 sulfuric acid (95%):hydrogen peroxide (30%) – *Caution – Strong oxidizer, use with extreme care*) for 1 h, rinsed with DI water, and then dried at 100°C for 2 h. A negative photoresist (AZ5214E) was used to define the overall pattern of the bottom electrode on glass. A 95 nm thick Au film, with a 5 nm Cr adhesion layer, was deposited by electron-beam evaporation (UNIVEX 450B, Oerlikon). After metal lift-off, a 50 nm thick $SiN_x$ layer was then deposited by plasma-enhanced chemical vapor deposition (PECVD 790, Plasma-Therm). Then the overall top electrode pattern was deposited perpendicular to and overlapping the bottom electrode using the same photolithography procedure. The area over of top and bottom electrode layer overlap was 180 μm x 180 μm. Next, an additional 200 nm thick $SiO_2$ layer was deposited over the whole surface to passivate the top surface. The substrate was exposed briefly to an $O_2$ plasma (Drytek RF Plasma asher, 1500W) to make the surface hydrophilic and then was immediately stored in DI water. Then a highly ordered polystyrene (PS) nanosphere monolayer was prepared at a liquid-air interface and was transferred to the substrate by emersing it at ~ 45° through the interface. Once the substrate was dried in air, $O_2$ plasma etching (Plasmatherm 790, 100W) was used to reduce the nanosphere size - with longer exposure times producing smaller final nanospheres. Then a metal nanopore mask was produced by depositing a 10 nm thick Cr film on top of the $SiO_2$ layer and then removing the PS nanospheres by sonication in chloroform or acetone for 5 min. Afterwards, a square pattern (150 μm x 150 μm) at the center of intersection area was defined by photolithography to act as an overall etch mask for subsequent dry etching. Finally, the RRDE arrays were produced by transferring the pattern through the template using multistep reactive ion etching (Plasmatherm 790). During etching, each upper layer acts as the etch mask for the layer below it, *e.g.*, the Cr layer protects the $SiO_2$ layer, the $SiO_2$ protects the Au layer, *etc*.

*Modeling and Calculations.* Modeling calculations were performed using finite element simulation software (COMSOL Multiphysics 5.0). The electrochemical system treated here is a simple outer-sphere heterogeneous electron transfer reaction at the electrodes, $O + ne^- \rightleftharpoons R$, where n is the number of electrons transferred. The arrays were simulated in a 2D geometry, consisting of recessed disk electrodes, a 50 nm thick insulating layer, a 100 nm thick ring electrode layer, and a 200 nm thick top insulator layer. The domain above the pores was drawn sufficiently large to avoid interference from boundaries, and the mesh was refined both within the nanopores and in the region just above the pores to avoid misleading results. For the case of high overpotential applied to the electrodes, constant-concentration boundary conditions were applied based on the assumption of complete oxidation or complete reduction on the electrode surfaces. The various devices were characterized at steady-state by assuming that the diffusion coefficients of the reduced and oxidized forms are the same, leading to the result that the sum of oxidized ($C_O$) and reduced ($C_R$) forms is constant over the diffusion space and is equal to the sum of the bulk concentrations ($C_{Bulk}$).

*Electrochemical Measurements.* Cyclic voltammetry (CV) experiments were performed with a CH Instruments electrochemical analyzer (Model 842C) using a Pt wire and Ag/AgCl as auxiliary and reference electrodes, respectively. The top and bottom electrodes of the RRDE arrays were operated as the first and second working electrodes. All potentials are reported *vs.* Ag/AgCl at 300K. Both the reference electrode and auxiliary electrode were immersed in a 200 µL solution inside a 8 mm diameter PDMS reservoir. In all CV measurements, the potential of the bottom electrodes was swept, and the top electrodes were either held at a constant potential (GC mode) or disconnected (non-GC mode).

## RESULTS AND DISCUSSION

*Fabrication of High Density Metal Nanopore Templates.* A key part of our strategy to study the electrochemical behavior of single molecules involves the preparation of high density arrays of zeptoliter-volume nanopores with internal annular ring and disk electrodes. Previous studies from our laboratory[17, 20] have demonstrated that the size of nanopore-embedded electrodes prepared by NSL is determined by the initial size of the polystyrene sphere and the duration and power of the subsequent $O_2$ plasma exposure. In order to produce elements with tunable size and spacing, here we utilized nanospheres with initial diameters ranging from 800 nm to 100 nm. Because the initial nanosphere diameter determines the site-to-site spacing in the final structure, starting with smaller diameter nanospheres produces higher density arrays. In addition, smaller initial size nanospheres can be processed using milder plasma treatment conditions to shrink the sphere size, thereby minimizing deformation of the nanospheres which can lead to non-uniform structures.

To test this fabrication scheme, nanospheres with initial diameters ranging from 800 nm, to 200 nm were first assembled on a glass slide and then exposed to an $O_2$ plasma in order to decrease the size of the nanospheres through isotropic etching.[37] **Figure 1** shows the dependence of the final nanosphere size on the duration of $O_2$ plasma etching. At shorter etching times, the average nanosphere size decreases monotonically with $O_2$ plasma exposure, and the resulting spheres exhibit smooth, spherical surfaces with the periodic structure of the nanosphere array being well preserved. At longer times ($t > 240$ s) the final nanosphere size becomes less sensitive to the etching time, and the surface of the resulting spheres is rougher. Based on these observations, the usable processing regime extends from the original diameter, $d_0$, to ~ $d_0/3$.

After shrinking the nanosphere size by $O_2$ plasma treatment, a 10 nm Cr layer was deposited uniformly over the etched nanosphere array. Then the nanospheres were removed by sonication in chloroform, revealing a Cr nanopore mask. Cr was chosen as an etch mask based on its good adhesion to $SiO_2$ (passivating layer for the electrochemical device) and its selectivity in subsequent dry etching steps. **Figure 2** shows scanning electron microscope (SEM) images of nanopore arrays with a variety of pore sizes and spacings. The pore size could be adjusted from 800 nm to 50 nm, and the pore density could be controlled from low (~ $10^8$ $cm^{-2}$) to high density (~ $10^{10}$ $cm^{-2}$) by varying the $O_2$ plasma exposure conditions and the initial size of nanospheres, respectively. At the smallest, $d_0 = 100$ nm, initial nanosphere diameter, the translational symmetry of the arrays was degraded relative to arrays produced from larger $d_0$ values. These images clearly demonstrate that NSL is a flexible, high-fidelity method to fabricate well-ordered, high-density nanopore arrays.

*Fabrication of High Density Dual Nanopore Electrode Arrays* (*NEAs*). Dual NEAs are nanopore arrays in which each nanopore has two electrodes, constructed in a metal-insulator-metal (MIM) structure in the vertical direction, as illustrated schematically in **Figure 3(A)**. First, the electrode pattern and the intersecting area of the two electrode layers, *i.e.* bottom disk electrode and top ring electrode, were defined by photolithography. The thicknesses of the metal and insulating layers were controlled by metal deposition and chemical vapor deposition, respectively. Then the metal nanopore template was fabricated on top of the intersecting electrodes. Finally, the dual NEAs were produced by dry etching to propagate the nanopore-templated pattern through to the bottom metal disk, at which the etch was stopped. Well ordered NEAs with tunable pore size and spacing were achieved at large scale, *viz*. **Figure 3(B)**. The cross-sectional SEM image, **Figure 3(C)**, shows the MIM structure in the NEA, each pore exhibiting from top to bottom: $SiO_2$ protection layer (grey), top Au ring electrode (white), $SiN_x$ insulating layer (black) and bottom Au disk electrode (white). The average bottom and top diameters for this particular conical structure are *ca.* 90 nm and 150 nm, respectively.

Considering that the combined thickness of the top Au layer and $SiN_x$ layer is ~150 nm, and that the nanopore shape is a right circular conical frustum, the effective volume of the ring-disk electrode region of each nanopore, *i.e.* the volume pertinent to redox cycling reaction is ~ $1.25 \times 10^{-18}$ L. Thus, the concentration corresponding to single molecule occupancy is ~ 1.3 μM. However, both the pore volume and the pore spacing are important for functional analysis of the electrochemical behavior of NEAs – the pore volume setting the single molecule occupancy criteria, and the pore spacing determining the ability to re-capture molecules that escape from a given pore in neighboring pores. The limitations on fabricating NEAs with high pore densities and small pore volumes by the NSL-templating strategy employed here arises due to the uniformity of the etching process when the top diameter of the nanopore is smaller than 100 nm. Additionally, the thickness of top $SiO_2$ layer is important to achieve uniform shapes and small diameter nanopore arrays. In order to balance pore density against the requirement to operate with well-structured nanopores for electrochemical measurements, the smallest initial nanosphere size used to fabricate NEAs for electrochemical measurements was 300 nm, corresponding to the image in **Figure 2(B)**. This design rule produces arrays with pore densities, $\rho_p$ ~$10^9$ $cm^{-2}$, which combined with an intersecting electrode area of 150 μm x 150 μm, leads to arrays with ~ 225,000 pores.

*Current Amplification in NEAs.* The unique geometry of the dual NEA, *i.e.* two individually addressable and closely spaced working electrodes within an ultrasmall volume nanopore, is a nearly ideal geometry for investigating the redox cycling reaction of small numbers of reversible electroactive species. Here, the bottom (disk) and top (ring) electrodes were used as generator and collector electrodes, respectively, during redox cycling experiments. Accordingly, species that are oxidized (reduced) at the bottom electrode can be reduced (oxidized) when efficiently captured by the top electrode. Furthermore, given the ~100 nm spacing between generator and collector, diffusion times between the electrodes for typical redox species in aqueous electrolyte are of the order of a few μs.

**Figure 4(A)** shows typical cyclic voltammograms (CVs) of $Ru(NH_3)_6^{2/3+}$ in 0.1 M KCl obtained by scanning the bottom electrode while floating (non-GC mode, black line) or holding the top electrode at +0.1V (GC mode, red line) or -0.4 V (GC mode, blue line) *vs.* Ag/AgCl on an array with 400 nm pore size and 460 nm pore-to-pore spacing. When operated in non-GC mode at a scan rate of 100 mV $s^{-1}$, the nanoscale RRDE array behaves like a single recessed microelectrode of the same electrode size (150 μm x 150 μm). Under non-GC mode conditions, a characteristic transport-limited CV (inset of **Figure 4(A)**) with substantial capacitive contribution was observed. This is likely due to the overlap of diffusion zones of neighboring nanopore electrodes.[40] Using a model developed by Bond *et.al.*,[41] a current of ~ 57 nA was calculated for a single recessed microelectrode of the same electrode size and depth as the nanoscale RRDE array. This value agrees well with the 56 nA peak current observed experimentally. When the potential of the top electrode was fixed to either a relatively reducing (-0.4 V) or oxidizing (0.1 V) value for $Ru(NH_3)_6^{2/3+}$, the limiting current of the RRDE array in GC-mode was significantly enhanced. The amplification of measurable current from 60 nA (solid, black line) to 3.30 μA (solid, red line) is clear evidence that the analyte undergoes redox cycling. The amplification factor for redox cycling ($AF_{RC}$), calculated from the ratio of limiting current in GC mode to that in non-GC mode, is $AF_{RC}$ = 55 under these conditions.

$AF_{RC}$ is strongly related to the collection efficiency of the generator-collector system, which is defined as the ratio of the limiting current at the collector electrode to that at the generator electrode. In the structures studied here, collection efficiencies for the top electrode, $\Phi_t$, as high as 99.4% ($d_0$ = 400 nm, 460 nm spacing, $E_{top}$ = +0.1 V) were measured. If the fixed potential of the top electrode is switched from +0.1 V to -0.4 V *vs.* Ag/AgCl, the analyte oxidized at the bottom electrode is then reduced at the top electrode. Under these conditions, the limiting currents for top and bottom electrodes were 3.51 μA (dashed blue line) and 3.47 μA (solid blue line), respectively, which gives the collection efficiency of the bottom electrode as $\Phi_b$ = 98.9%. Based on the theory of Tabei and coworkers,[25] the number of redox cycles $N_{RC}$ can be estimated from,

$$N_{RC} = \frac{1}{1-\Phi_t\Phi_b} \tag{1}$$

For the nanoscale RRDE array described above, $\Phi_t$ and $\Phi_b$ were 99.4% and 98.9%, respectively, yielding $N_{RC}$ = 57.7, in excellent agreement with the experimentally measured value of $AF_{RC}$. This value is substantially higher than previously reported $AF_{RC}$ values obtained from lower density RRDE arrays,[19] an observation that can be attributed to the higher array density and smaller pore size, both of which work to improve the redox cycling efficiency.

**Figure 4(B)** shows simulated CVs of nanoscale RRDE arrays with the same geometric parameters as the experimental structure, with the top electrode held at +0.1V (red line), -0.4 V (blue line) or floating (black line). The simulated single-nanopore limiting current (~ 15 pA) is somewhat smaller than the experimental value (~30 pA) obtained through dividing the total limiting current (3.30 μA) by the number of nanopores (~112,500) on the array. The simulated amplification factor $AF_{sim}$ = 54.8 calculated from the ratio of the simulated limiting currents in GC mode to that in non-GC mode agrees very well with the experimental $AF_{RC}$ = 55. The calculated spatial distributions of redox species under different applied potentials are shown in **Figures 4(C)** and **4(D)**, with the top ring electrode potential held at +0.1 V and -0.4 V *vs.* Ag/AgCl, respectively. With the top electrode set at an oxidizing potential, **Figure 4(C)**, $Ru(NH_3)_6^{2+}$ reduced at the bottom disk electrode is efficiently oxidized to $Ru(NH_3)_6^{3+}$ at the top ring electrode. Interestingly, the simulated spatial distributions reveal pockets of unreacted $Ru(NH_3)_6^{3+}$ near the surface of the insulator in **Figure 4(C)**. Conversely, when the top electrode is set to a negative potential (-0.4 V), **Figure 4(D)**, $Ru(NH_3)_6^{3+}$ produced at the bottom electrode is reduced at the top electrode.

*Effect of Pore Size and Spacing.* The characteristic collision times of molecules with the electrodes inside the nanopores depends strongly on pore size. On the other hand, the recapture of escaped molecules by adjacent nanopore-embedded electrodes depends largely on pore density. Thus, the collection efficiency and the current amplification should depend strongly on the geometry of the array. Both experiments and simulations were conducted to understand the dependence of RC response on the nanopore geometry, especially the effect of pore size and pore density, on the efficiency of redox cycling.

**Table 1** shows the experimental and simulated AF values for nanoscale RRDE arrays with different pore spacings, $S_p$. A series of nanoscale RRDE arrays were fabricated by using nanospheres with different initial diameters (800 nm, 600 nm, 460 nm), each template being reduced to the same sphere size (~ 200 nm) by $O_2$ plasma etching to produce a series of structures with constant pore size but varying pore density. The electrochemical behavior of these structures was then compared to finite element simulations performed to probe the effect of pore spacing on AF. As shown in **Table 1**, both simulated and experimental AF values increase with decreasing pore spacing. This is likely due to overlapping diffusion zones on high density nanoscale RRDE arrays, as is evident in the simulated concentration distributions in **Figures 4(C)** and **4(D)**. At high pore densities the overlapping diffusion zones improve the collection efficiency by recapturing any molecules that escape from a neighboring nanopore.

The dependence of AF on pore size was also investigated on a series of nanoscale RRDE arrays of constant pore spacing but different pore diameters. These structures were prepared by starting from NSL templates with the same initial nanosphere diameter, but then exposing them to $O_2$ plasma for differing times to produce different final pore diameters. The simulated and experimental AF values of this series are summarized in **Table 2**. Both show that AF increases with increasing nanopore diameter, reflecting a larger net capture efficiency for larger pores, thus giving rise to larger $AF_{RC}$. At these small sizes, this likely reflects the effect of $\Phi_b$, which increases at larger disk electrode sizes. This was confirmed by simulations which illustrate that $\Phi_b$ increases with increasing nanopore diameter (**Table 2**).

*Linear Response and Scan Rate Dependence.* In order to test the performance of the high density nanopore electrode arrays to small molecular loadings, the whole array was operated in GC mode to detect redox species of $Ru(NH_3)_6^{3+}$ at concentrations down to 100 nM. The limiting voltammetric current obtained from $Ru(NH_3)_6^{3+}$ as a function of concentration in GC mode is displayed in **Figure 5(A)**, illustrating that it is linear over 5 orders of magnitude in concentration. The current signals in these experiments were collected from a 150 μm x 150 μm nanopore electrode array with a (top) pore diameter and spacing 150 nm and 300 nm, respectively. In this geometry, the conical frustum gives an average pore diameter ~ 150 nm at the top and ~90 nm at the bottom. Considering that the combined thickness of the top Au and $SiN_x$ layers is 150 nm, the effective volume for redox cycling reaction is 1.25 aL. In order to obtain single molecule occupancy, the required concentration of analyte is ~ 1.3 μM. As shown in **Figure 5(A)**, the limiting current at 1 μM was ~ 0.4 nA, which means on average each nanopore produced ~ 1.8 fA current signal under these conditions (~ 225,000 pores on the entire array) corresponding to *ca.* $10^4$ electron transfer events per second, a realistic value given an estimated diffusion time of 10 μs. This value is ~10x smaller than the value (20 fA) reported by Lemay and coworkers from single molecule diffusion inside an opposed-planar electrode nanofluidic electrochemical device.[32] We attribute this to the lower collection efficiency of the open geometry of nanopore electrodes compared to the closed structure used by Lemay's group.

Another advantage of high density nanopore electrode arrays is the small capacitive current in GC mode, as shown in **Figure 5(B)**. At high electrolyte concentrations, such as those used here, the magnitude of the charging current for nanoelectrodes is typically comparable to the faradaic current at low analyte concentrations. Here, the measured charging current at both the top and bottom electrode increases linearly with the scan rate ranging from 0.1 V/s to 100

V/s, *viz*. **Figure 5(B)** *inset*. However, the capacitance of the whole array had little effect on the voltammetric signal when the scan rate was below 1 V/s. The smaller capacitive current (~ 0.2 nA) of the top electrode even at scan rates as high as 100 V $s^{-1}$ indicates that these devices may serve as a suitable electrode platforms for ultrafast electrochemistry, as well as single molecule, measurements.

## CONCLUSION

In this work we demonstrate a simple and robust approach to fabricate high density nanopore arrays with well-controlled dual-electrodes for ultrahigh efficiency redox cycling. Nanosphere lithography and $O_2$ plasma etching are clearly competent to fabricate nanopore arrays with controlled pore diameter and spacing over a wide range. Electrochemical reactions of redox couples operated in generator and collector mode produced greatly enhanced currents relative to non-GC operation, with collector electrode collection efficiencies as high as $\Phi_t$ = 99.4%. Both experiments and simulations illustrate the significance of pore size and spacing in determining high performance redox cycling.

The nanoscale RRDE arrays developed and studied here represent a new part of electrochemical phase space, where the small electrochemical detection volume (~1 aL) of each nanopore means that single molecule occupancy can be achieved at μM concentrations. In fact, at the lowest concentration at which a chemically significant electrochemical signal was measured (100 nM), the average occupancy was <n> ~ 0.13. This measurement was enabled by a combination of high redox cycling collection efficiency at both bottom and top electrodes, $\Phi_{b,t}$ ~ 99%, and a massively parallel array of 2.25 x $10^5$ pores giving rise to aggregate signals significantly above the noise level. Furthermore, these large area nanoscale RRDE arrays exhibit insignificant charging current at scan rates below 1 V $s^{-1}$ and acceptable charging currents at scan rates as high as 100 V $s^{-1}$, suggesting their use for simultaneous ultrafast, ultrasensitive electrochemical measurements.

## ACKNOWLEDGMENT

This work was supported by the National Science Foundation grant 1404744 (K.F. and C.M.) and the Defense Advanced Research Projects Agency FA8650-15-C-7546 (D.H.). Fabrication and structural characterization of the devices studied here were accomplished at the Notre Dame Nanofabrication Facility and the Notre Dame Integrated Imaging Facility, whose generous support is gratefully acknowledged.

## REFERENCES

1 Arrigan, D. W. M. *Analyst* 2004**, 129**, (12), 1157-1165.

2 Cox, J. T.; Zhang, B. *Ann. Rev. Anal. Chem.* 2012**, 5**, (1), 253-272.

3 Oja, S. M.; Wood, M.; Zhang, B. *Anal. Chem.* 2013**, 85**, (2), 473-486.

4 Oja, S. M.; Fan, Y.; Armstrong, C. M.; Defnet, P.; Zhang, B. *Anal. Chem.* 2016**, 88**, (1), 414-430.

5 Dawson, K.; O'Riordan, A. *Ann. Rev. Anal. Chem.* 2014**, 7**, (1), 163-181.

6 Murray, R. W. *Chem. Rev.* 2008**, 108**, (7), 2688-2720.

7 Krapf, D.; Wu, M.-Y.; Smeets, R. M. M.; Zandbergen, H. W.; Dekker, C.; Lemay, S. G. *Nano Lett.* 2006**, 6**, (1), 105-109.

8 Wang, G.; Zhang, B.; Wayment, J. R.; Harris, J. M.; White, H. S. *J. Am. Chem. Soc.* 2006**, 128**, (23), 7679-7686.

9 Ivanov, A. P.; Freedman, K. J.; Kim, M. J.; Albrecht, T.; Edel, J. B. *ACS Nano* 2014**, 8**, (2), 1940-1948.

10 Cheng, W.; Dong, S.; Wang, E. *Anal. Chem.* 2002**, 74**, (15), 3599-3604.

11 Menon, V. P.; Martin, C. R. *Anal. Chem.* 1995**, 67**, (13), 1920-1928.

12 Lanyon, Y. H.; De Marzi, G.; Watson, Y. E.; Quinn, A. J.; Gleeson, J. P.; Redmond, G.; Arrigan, D. W. M. *Anal. Chem.* 2007**, 79**, (8), 3048-3055.

13 Sandison, M. E.; Cooper, J. M. *Lab Chip* 2006**, 6**, (8), 1020-1025.

14 Santoro, F.; Dasgupta, S.; Schnitker, J.; Auth, T.; Neumann, E.; Panaitov, G.; Gompper, G.; Offenhäusser, A. *ACS Nano* 2014**, 8**, (7), 6713-6723.

15 LaFratta, C. N.; Walt, D. R. *Chem. Rev.* 2008**, 108**, (2), 614-637.

16 Ma, C.; Contento, N. M.; Gibson, L. R.; Bohn, P. W. *Anal. Chem.* 2013**, 85**, (20), 9882-9888.

17 Ma, C.; Xu, W.; Wichert, W. R. A.; Bohn, P. W. *ACS Nano* 2016**,** 10.1021/acsnano.6b00049.

18 Ma, C.; Zaino Iii, L. P.; Bohn, P. W. *Chem. Sci.* 2015**, 6**, (5), 3173-3179.

19 Ma, C.; Contento, N. M.; Bohn, P. W. *J. Am. Chem. Soc.* 2014**, 136**, (20), 7225-7228.

20 Ma, C.; Contento, N. M.; Gibson, L. R.; Bohn, P. W. *ACS Nano* 2013**, 7**, (6), 5483-5490.

21 Han, D. H.; Zaino, L. P.; Fu, K. Y.; Bohn, P. W. *J. Phys. Chem. C* 2016**,** submitted.

22 Barnes, E. O.; Lewis, G. E. M.; Dale, S. E. C.; Marken, F.; Compton, R. G. *Analyst* 2012**, 137**, (5), 1068-1081.

23 Frumkin, A.; Nekrasov, L.; Levich, B.; Ivanov, J. *J. Electroanal. Chem.* 1959**, 1**, (1), 84-90.

24 Bruckenstein, S.; Miller, B. *Acc. Chem. Res.* 1977**, 10**, (2), 54-61.

25 Niwa, O.; Morita, M.; Tabei, H. *Anal. Chem.* 1990**, 62**, (5), 447-452.

26 Bard, A. J.; Crayston, J. A.; Kittlesen, G. P.; Varco Shea, T.; Wrighton, M. S. *Anal. Chem.* 1986**, 58**, (11), 2321-2331.

27 Goluch, E.; Wolfrum, B.; Singh, P.; Zevenbergen, M. G.; Lemay, S. *Anal. Bioanal. Chem.* 2009**, 394**, (2), 447-456.

28 Fan, F.-R. F.; Bard, A. J. *Science* 1995**, 267**, (5199), 871-874.

29 Bard, A. J.; Fan, F.-R. F. *Acc. Chem. Res.* 1996**, 29**, (12), 572-578.

30 Fan, F.-R. F.; Kwak, J.; Bard, A. J. *J. Am. Chem. Soc.* 1996**, 118**, (40), 9669-9675.

31 Zevenbergen, M. A. G.; Krapf, D.; Zuiddam, M. R.; Lemay, S. G. *Nano Letters* 2006**, 7**, (2), 384-388.

32 Zevenbergen, M. A. G.; Singh, P. S.; Goluch, E. D.; Wolfrum, B. L.; Lemay, S. G. *Nano Letters* 2011**, 11**, (7), 2881-2886.

33 Li, T.; Su, L.; Hu, W.; Dong, H.; Li, Y.; Mao, L. *Anal. Chem.* 2010**, 82**, (4), 1521-1526.

34 Huske, M.; Stockmann, R.; Offenhausser, A.; Wolfrum, B. *Nanoscale* 2014**, 6**, (1), 589-598.

35 Fischer, U. C.; Zingsheim, H. P. *J. Vac. Sci. Technol.* 1981**, 19**, (4), 881-885.

36 Plettl, A.; Enderle, F.; Saitner, M.; Manzke, A.; Pfahler, C.; Wiedemann, S.; Ziemann, P. *Adv. Funct. Mater.* 2009**, 19**, (20), 3279-3284.

37 Ji, L.; Chang, Y.-F.; Fowler, B.; Chen, Y.-C.; Tsai, T.-M.; Chang, K.-C.; Chen, M.-C.; Chang, T.-C.; Sze, S. M.; Yu, E. T.; Lee, J. C. *Nano Lett.* 2014**, 14**, (2), 813-818.

38 Moon, G. D.; Lee, T. I.; Kim, B.; Chae, G.; Kim, J.; Kim, S.; Myoung, J.-M.; Jeong, U. *ACS Nano* 2011**, 5**, (11), 8600-8612.

39 Whitney, A. V.; Myers, B. D.; Van Duyne, R. P. *Nano Lett.* 2004**, 4**, (8), 1507-1511.

40 Wahl, A.; Dawson, K.; MacHale, J.; Barry, S.; Quinn, A. J.; O'Riordan, A. *Faraday Discuss.* 2013**, 164**, (0), 377-390.

41 Bond, A. M.; Luscombe, D.; Oldham, K. B.; Zoski, C. G. *J. Electroanal. Chem. Interf. Electrochem* 1988**, 249**, (1), 1-14.